

# Steady Flow in a Patient-Averaged Inferior Vena Cava—Part II: Computational Fluid Dynamics Verification and Validation

BRENT A. CRAVEN <sup>1</sup>, KENNETH I. AYCOCK,<sup>1</sup> and KEEFE B. MANNING<sup>2</sup>

<sup>1</sup>Division of Applied Mechanics, Office of Science and Engineering Laboratories, Center for Devices and Radiological Health, United States Food and Drug Administration, Silver Spring, MD, USA; and <sup>2</sup>Department of Biomedical Engineering, Pennsylvania State University, University Park, PA, USA

(Received 23 July 2018; accepted 27 October 2018; published online 16 November 2018)

Associate Editors Dr. David A. Steinman, Dr. Francesco Migliavacca, and Dr. Ajit P. Yoganathan oversaw the review of this article.

## Abstract

**Purpose**—The embolus trapping performance of inferior vena cava (IVC) filters critically depends on how emboli flow through the IVC and, thereby, on the underlying hemodynamics. Most previous studies of IVC hemodynamics have used computational fluid dynamics (CFD), but few have validated their results by comparing with quantitative experimental measurements of the flow field and none have validated in an anatomical model of the IVC that includes the primary morphological features that influence the hemodynamics (iliac veins, infrarenal curvature, and non-circular vessel cross-section). In this study, we perform verification and validation of CFD simulations in a patient-averaged anatomical model of the IVC.

**Methods**—Because we are most interested in the fluid dynamics that influence embolus transport and IVC filter embolus trapping, we focus our analyses on the velocity distribution and the amount of swirl and mixing in the infrarenal IVC. A rigorous mesh refinement study is first conducted at the highest flow rate condition to verify the computed solutions. To validate the CFD predictions of the flow patterns, we then compare with particle image velocimetry (PIV) data acquired in the same model in two planes (coronal and sagittal) within the infrarenal IVC at two flow rates corresponding to rest and exercise conditions.

**Results**—Using unstructured hexahedral meshes ranging in size from 800,000 to 102.5 million computational cells, we demonstrate that a coarse mesh may be used to resolve the gross flow patterns and velocity distribution in the IVC. A finer mesh is, however, required to obtain asymptotic mesh convergence of swirl and mixing in the IVC, as quantified by the local normalized helicity,  $LNH$ , and the volume-averaged helicity intensity,  $\overline{HI}$ . Based on the results of the mesh refinement study, we use a moderately fine mesh containing approximately 26 million cells for comparison with experimental data. The validation study demonstrates excellent

qualitative agreement between CFD predictions and PIV measurements of the velocity field at both conditions. Quantitatively, we show that the global relative comparison error,  $E$ , between CFD and PIV ranges from 3 to 11%. By performing sensitivity studies, we demonstrate that the quantitative discrepancy is attributable to a combination of uncertainty in the inlet flow rates and uncertainty associated with precisely aligning the PIV data with the CFD geometry. **Conclusions**—Overall, the study demonstrates mesh-convergent CFD simulations that predict IVC flow patterns that agree reasonably well with PIV data, even at exercise conditions where the flow in the IVC is extremely complex.

**Keywords**—Inferior vena cava, Hemodynamics, Computational fluid dynamics, Verification and validation.

## INTRODUCTION

The inferior vena cava (IVC) is a large vein in the thoracic-abdominal cavity through which blood returns to the heart from the lower extremities (Fig. 1). IVC filters are medical devices implanted in the IVC to capture emboli to prevent them from passing to the right side of the heart and the downstream pulmonary arteries, where they can become lodged and cause a condition known as pulmonary embolism that is often fatal. The embolus trapping performance of an IVC filter critically depends on how emboli flow through the IVC and, thereby, on the underlying hemodynamics.

Most previous studies of IVC hemodynamics have used computational fluid dynamics (CFD) (e.g., Refs. 3–6, 14, 21, 23, 24, 32–34, 36–39). However, few studies have validated computational predictions by comparing with quantitative experimental measurements of the flow field. Stewart *et al.*<sup>36</sup> and Nicolás *et al.*<sup>21</sup> both compared with particle image velocimetry

Address correspondence to Brent A. Craven, Division of Applied Mechanics, Office of Science and Engineering Laboratories, Center for Devices and Radiological Health, United States Food and Drug Administration, Silver Spring, MD, USA. Electronic mail: brent.craven@fda.hhs.gov

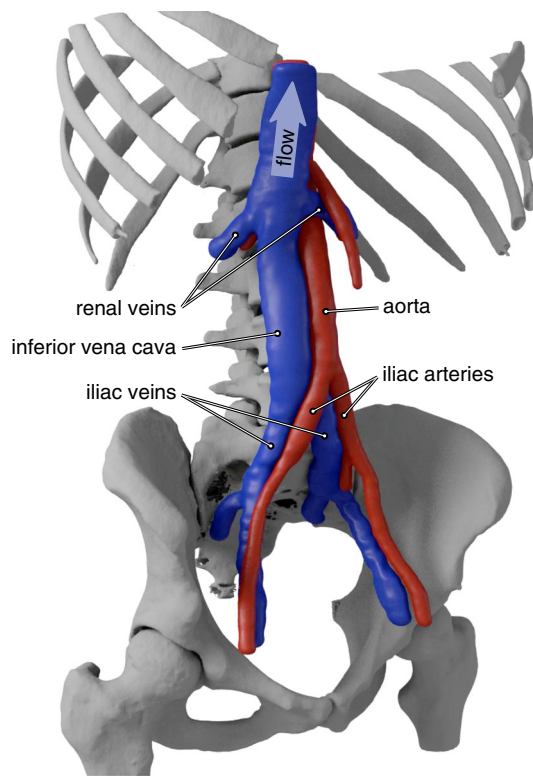


**FIGURE 1. Anatomy of the human inferior vena cava (IVC) reconstructed from patient computed tomography (CT) data.<sup>4</sup> The IVC is located in the thoracic-abdominal cavity, downstream of the confluence of the iliac veins.**

(PIV) data to validate their CFD simulations, which were performed at a flow rate corresponding to resting conditions using a circular, straight-tube model of the IVC. Tedaldi *et al.*<sup>38</sup> compared CFD predictions with PIV measurements in a more realistic IVC model that included iliac veins, though it was idealized and did not include infrarenal curvature or a non-circular cross-section, both of which can influence the hemodynamics.<sup>4</sup> To our knowledge, there has been no study to date that has validated CFD predictions of hemodynamics in an anatomical model of the IVC that includes the primary morphological features that influence the hemodynamics (iliac veins, infrarenal curvature of the IVC, and non-circular vessel cross-section; see Fig. 1).

The objective of this study is to perform CFD simulations of the flow in an anatomical model of the IVC and to validate the predictions by comparing with PIV data in the same model.<sup>11</sup> We perform CFD simulations using the open-source computational continuum mechanics library OpenFOAM. A mesh refinement study is first conducted to verify that the solutions are mesh-convergent and to quantify the numerical uncertainty. The CFD predictions are then compared with PIV data in two planes (coronal and sagittal) within the infrarenal IVC at two flow rates

corresponding to rest and exercise conditions. Finally, the implications of the results regarding IVC filter embolus trapping are discussed.

## MATERIALS AND METHODS

### *Verification and Validation Terminology*

To avoid the potential for confusion concerning the use of the terms “verification” and “validation,” we first clarify terminology. According to Roache,<sup>28</sup> in general, *verification is the process of ensuring that the governing equations are solved correctly and validation ensures that the correct governing equations are being solved.* That is, verification is purely an applied mathematics exercise that seeks to evaluate the error implicit in the numerical solution of the governing equations.<sup>29</sup> In contrast, the goal of validation is to compare numerical simulations with experiments to assess the degree to which the underlying governing equations that are being solved accurately represent the real world.

In general, there are two parts to verification: (i) code verification, and (ii) solution (or calculation) verification. Code verification is performed to ensure that the underlying mathematical model has been implemented correctly and that the theoretical order of accuracy of the numerical method is obtained, nominally using the method of manufactured solutions (MMS).<sup>22,28</sup> Solution verification is the process of computing solutions using a consistently and uniformly refined series of meshes to ensure that the CFD simulations are mesh-convergent and that the results are insensitive to further mesh refinement. More rigorously, solution verification also includes using Richardson extrapolation techniques<sup>1,22,28</sup> to quantitatively estimate the numerical uncertainty in the solution due to discretization error. Important to the present study, when performing solution verification using unstructured CFD meshes, quantitative evaluation of numerical uncertainty estimates is often restricted to global or integrated quantities. Richardson extrapolation techniques can be used to estimate the local numerical uncertainty in the solution field variables on a point-wise basis when using structured CFD meshes for simple geometries because mesh refinement (or coarsening) can be highly controlled to ensure that the location of cell centers (or nodes) is the same between meshes. However, due to the lack of control in specifying the exact spatial location of computational cells in an unstructured mesh, using Richardson extrapolation techniques to estimate local numerical uncertainty of the solution field variables in the domain is extremely challenging. Consequently, inte-

grated quantities of interest are typically used to evaluate the numerical uncertainty of CFD solutions on unstructured meshes.

In validating a computational model, the comparison of simulation results with experiments can take varying forms depending on the rigor of the comparison.<sup>2</sup> From least to most rigorous, this may include: visual qualitative comparison of numerical and experimental output (e.g., field contours), quantitative comparison of deterministic predictions with a single experimental measurement at nominal conditions, or statistical comparison of non-deterministic simulation results with distributions of experimental measurements and the calculation of a quantitative validation metric (e.g., see Refs. 10, 30). In general, the overall credibility of the validation is commensurate with the rigor of the comparison.

### Geometry

The present IVC geometry (Fig. 2) is based on the patient-averaged model of Rahbar *et al.*,<sup>23</sup> which was constructed from measurements of normal IVC anat-

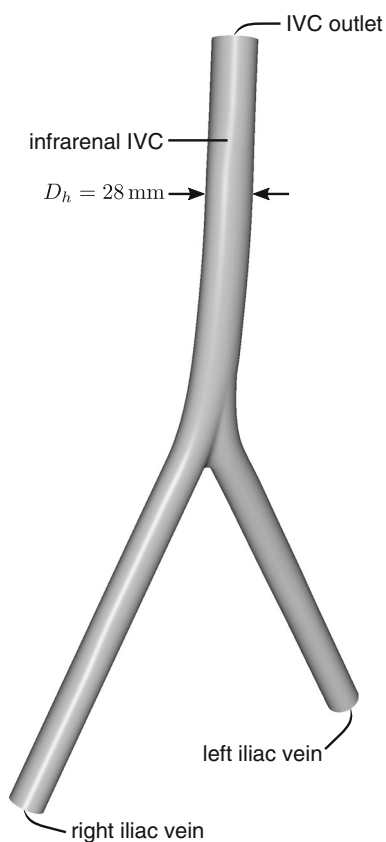


**FIGURE 2.** Patient-averaged IVC geometry used for CFD based on the model of Rahbar *et al.*<sup>23</sup> with several modification (see the text for details). The average hydraulic diameter,  $D_h$ , of the infrarenal IVC is 28 mm.

omy from computed tomography (CT) data in 10 patients. While the patient-averaged IVC model is simplified compared to a patient-specific model (e.g., see Ref. 4), it possesses the primary morphological features that influence the hemodynamics (iliac veins, infrarenal curvature of the IVC, and non-circular vessel cross-section) and it is more complex than previous experimental models used to quantify IVC hemodynamics.

As described by Gallagher *et al.*,<sup>11</sup> the patient-averaged model of Rahbar *et al.*<sup>23</sup> was modified in several ways to accommodate the present study. First, the model was uniformly scaled to obtain an average hydraulic diameter of 28 mm in the infrarenal IVC, which is representative of the maximum indicated IVC diameter for most commercially available IVC filters. This diameter was chosen because it represents the worst-case for embolus trapping due to the larger unobstructed area when the filter is implanted.

Second, we truncated the IVC model just inferior to (i.e., upstream of) the renal veins. This is because we are interested in the hemodynamics in the infrarenal IVC and the flow patterns that influence embolus trapping. In general, renal vein entry angles are less than  $90^\circ$ ,<sup>39</sup> as they are in the patient-averaged IVC (see Ref. 4). Thus, the renal inflow is vectored downstream and does not generally influence the upstream flow inferior to the renal veins except perhaps in the immediate vicinity of the renal vein confluence. This has been confirmed in previous work by Wang and Singer,<sup>39</sup> who found that “renal inflow impacts only the flow field downstream of the renal veins.” Because IVC filters are typically placed in the infrarenal IVC,<sup>8</sup> renal vein inflow is not generally expected to influence IVC filter embolus trapping. Thus, to simplify both the experiments<sup>11</sup> and the present CFD simulations, we omit the renal veins.

Third, and finally, both the left and right iliac veins were extended, or “lofted,” to a circular cross-section. The iliac veins in the patient-averaged model of Rahbar *et al.*<sup>23</sup> have a cross-section that is slightly elliptical. To simplify the specification of boundary conditions in the CFD simulations, in fabricating the patient-averaged model using inkjet 3D printing,<sup>7</sup> we designed the upstream inlets to the iliac veins to obtain fully developed flow at both flow conditions (rest and exercise). This was accomplished by extending (or “lofting”) the elliptical cross-section of each iliac inlet to a circular cross-section of diameter 2.4 cm over a distance of 5 cm, resulting in a smooth transition between the two cross-sections (see Ref. 11 for further details). The 5 cm circle-to-ellipse transition and an additional 9 cm upstream circular section were fabricated as part of the patient-averaged model<sup>11</sup> and are included in the geometric model used for CFD (Fig. 2).

In the experiments,<sup>11</sup> straight inlet tubes of 2.4 cm inner diameter with a length of 1.22 m were attached to the model to obtain fully developed flow into each iliac vein at both rest and exercise flow rates (see Section “[Experimental Conditions](#)”).

### Experimental Conditions

As detailed by Gallagher *et al.*<sup>11</sup> and summarized in Table 1, experiments were performed using the 3D printed patient-averaged model at two flow rates corresponding to rest and exercise conditions (1 and 6 L/min, respectively) with a mixture of water, sodium iodide (NaI), and glycerol as the working fluid. PIV measurements were acquired in two planes (coronal and sagittal) in the inlet to both iliacs and in the infrarenal section of the IVC. The temperature of the working fluid was monitored during the experiments, and the fluid density and viscosity were measured as a function of temperature to specify the value of each at both conditions (Table 1).

The working fluid used in the experiments was Newtonian. Initial attempts to develop a non-Newtonian blood analog fluid with a high index of refraction using a mixture of water, NaI, glycerol, and xanthan gum (XG) failed due to the interaction of NaI and XG. As recently reported by Najjari *et al.*,<sup>20</sup> Gallagher *et al.*<sup>11</sup> found that the large amount of NaI required to obtain a refractive index of 1.51 to match the 3D printed model considerably reduced the shear-thinning properties that are normally imparted by the addition of XG. After numerous attempts, they were unable to match both the refractive index of the model and the shear-thinning, non-Newtonian characteristics of blood. Because of this, Gallagher *et al.*<sup>11</sup> instead used a Newtonian mixture of water, NaI, and glycerol as the working fluid.

### Computational Mesh

Eight computational meshes were generated to perform a rigorous mesh refinement study to ensure

**TABLE 1. Summary of the fluid properties and flow conditions from the experiments of Gallagher *et al.*<sup>11</sup>**

Parameter	Condition	
	Rest	Exercise
Kinematic viscosity, $\nu$ ( $m^2/s$ )	$3.21 \times 10^{-6}$	$3.02 \times 10^{-6}$
Density, $\rho$ ( $kg/m^3$ )	1817	1817
Left iliac flow rate (L/min)	0.5	3.0
Right iliac flow rate (L/min)	0.5	3.0
IVC flow rate (L/min)	1.0	6.0
IVC Reynolds number, $Re$	236	1504
IVC Dean number, $De$	28	175

that the computed solutions are mesh-convergent. The *cfMesh* utility available in OpenFOAM (version 1712; OpenCFD Ltd., Bracknell, UK) was used to generate unstructured hexahedral meshes with a uniform cell size in the core of the vessel lumen and with five wall-normal layers to resolve large, near-wall velocity gradients. As summarized in Table 2, the eight CFD meshes (Meshes 1–8) were created with each successive (finer) mesh having approximately twice the number of computational cells as the preceding (coarser) mesh. This yielded a series of eight uniformly refined meshes having between 800,000 and 102.5 million computational cells for the coarsest and finest meshes, respectively. A subset of the CFD meshes are shown in Fig. 3.

### Governing Equations

Here, we assume the laminar incompressible flow of a Newtonian fluid that is governed by the incompressible continuity

$$\nabla \cdot \mathbf{u} = 0 \quad (1)$$

and Navier–Stokes equations

$$\frac{\partial \mathbf{u}}{\partial t} + (\mathbf{u} \cdot \nabla) \mathbf{u} = -\frac{\nabla p}{\rho} + \nu \nabla^2 \mathbf{u} \quad (2)$$

where  $\mathbf{u}$  is the velocity vector,  $p$  is pressure,  $\rho$  is density, and  $\nu$  is the kinematic viscosity. The incompressible and Newtonian fluid approximations are justified by the use of a Newtonian liquid as the working fluid in the experiments (see Section “[Experimental Conditions](#)”). We assume laminar flow based on the maximum Reynolds number that occurs in the model under both rest and exercise conditions (approximately 240 and 1500, respectively). Though 1500 is a moderately large Reynolds number for laminar flow in a branching vessel, care was taken in the design of the upstream inlet tubing to provide a well-conditioned, fully developed laminar flow to each iliac vein. This pre-

**TABLE 2. Summary of the number of computational cells and the uniform mesh spacing,  $\Delta$ , in the core of the vessel lumen for each CFD mesh.**

Mesh	No. cells ( $\times 10^6$ )	$\Delta$ ( $\mu m$ )
1	0.80	1036
2	1.60	786
3	3.20	600
4	6.40	461
5	12.80	356
6	25.59	276
7	51.16	215
8	102.5	168



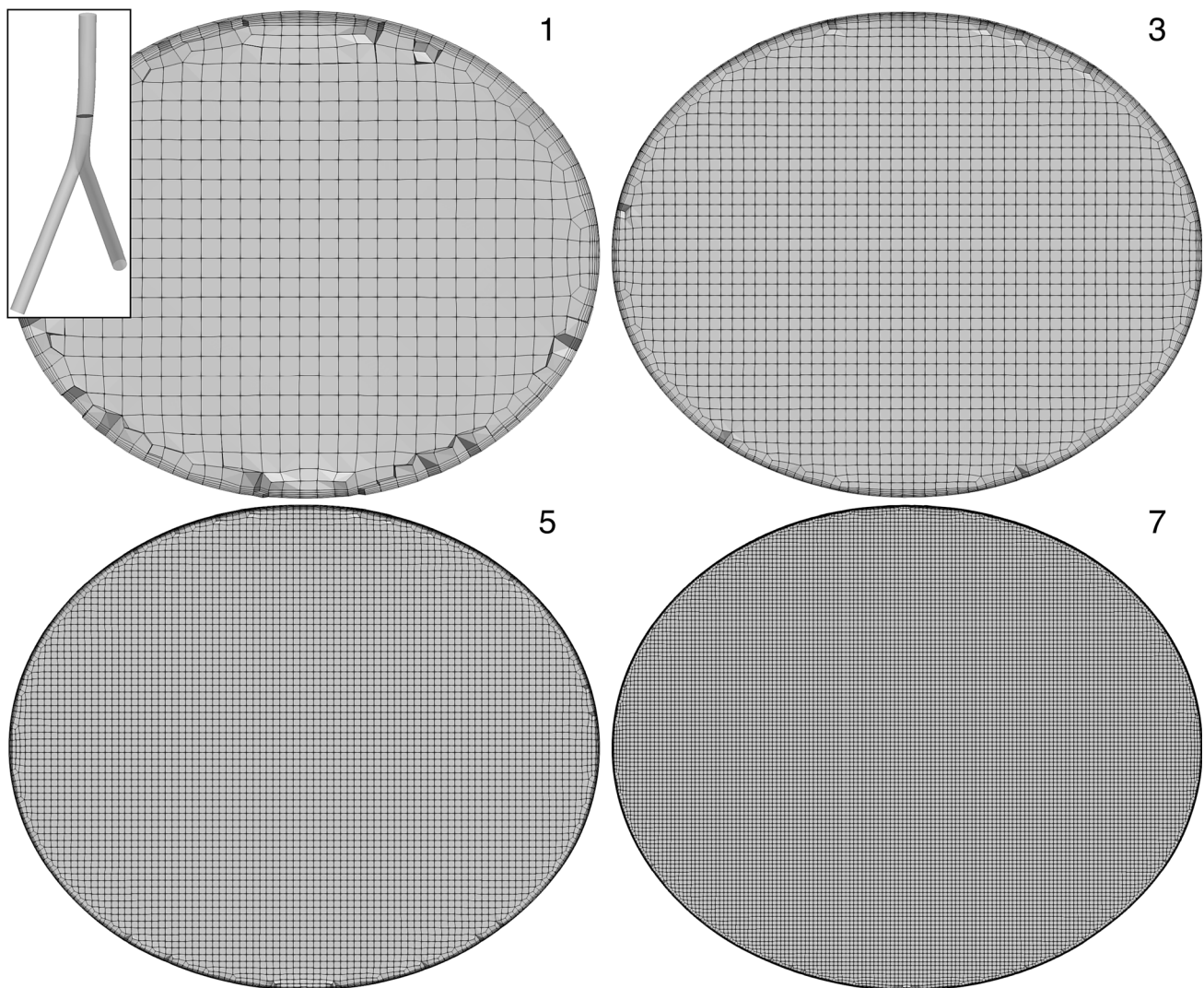


**FIGURE 3.** Unstructured hexahedral CFD meshes. A transverse cross-section of Meshes 1, 3, 5, and 7 (see Table 2) in the infrarenal IVC at the location illustrated in the inset. The size of the meshes ranges from 0.8 million to 102.5 million computational cells for the coarsest (Mesh 1) and finest (Mesh 8) meshes, respectively.

vented upstream disturbances that might otherwise cause transition to occur in the downstream infrarenal IVC, where the maximum Reynolds number occurs. Our assumption of laminar flow is in accord with the experimental measurements of Roach *et al.*,<sup>25</sup> who measured critical Reynolds numbers for transition to turbulence in a series of reverse bifurcations. For a reverse bifurcation angle comparable to that in the patient-averaged IVC ( $57^\circ$ ), the critical Reynolds number for steady flow is about 1800.<sup>25</sup> Most importantly, however, as described by Gallagher *et al.*,<sup>11</sup> the laminar flow assumption was confirmed in the PIV experiments in the present geometry at both flow conditions (rest and exercise).

#### *Boundary Conditions*

As mentioned in Section “**Geometry**”, the length of the straight section of upstream tubing (1.22 m) was such that fully developed laminar flow occurs at the inlet to each iliac vein at both rest and exercise conditions. The presence of fully developed flow was confirmed from PIV measurements of the velocity distribution in the round inlet section of each iliac.<sup>11</sup> This greatly simplified the specification of inlet velocity boundary conditions for CFD, which consisted of imposing the analytical solution for circular Poiseuille flow as a function of the flow rate at each inlet—i.e.,

$$u_n = \frac{2Q}{A} \left( 1 - \frac{r^2}{R^2} \right) \quad (3)$$

where  $u_n$  is the normal velocity to the inlet patch,  $Q$  is the volumetric flow rate,  $A$  and  $R$  are the respective area and radius of the inlet patch, and  $r$  is the distance from the centroid of the patch to each face center where the velocity is imposed. A uniform fixed relative pressure boundary condition of  $p = 0$  was applied at the outlet and a zero-gradient Neumann condition was applied for pressure at both iliac inlets. The *pressureInletOutletVelocity* boundary condition available in OpenFOAM was used for velocity at the outlet, which is a local boundary condition applied at each face center based on the sign of the flux. A zero-gradient Neumann condition is applied on patch faces where there is outflow, and an extrapolated Dirichlet condition is applied on patch faces in the event of inflow. Finally, no-slip boundary conditions were applied on the rigid walls of the IVC.

### Numerical Methods

Steady-state numerical solutions of the incompressible continuity (Eq. 1) and Navier–Stokes (Eq. 2) equations were computed in OpenFOAM (version 1712) using the “consistent” formulation of the Semi-Implicit Method for Pressure-Linked Equations algorithm (SIMPLEC) with second-order accurate spatial discretization schemes. Iterative convergence of the solutions was ensured by forcing the normalized residuals for velocity and pressure to be less than  $1 \times 10^{-12}$ . Additionally, we monitored several solution quantities (e.g., outlet flow rate, average pressure at both iliac inlets, maximum velocity, minimum and maximum pressure in the domain) throughout the simulation to confirm iterative convergence. A converged steady-state solution was computed for each case on a high-performance computing (HPC) system at the U.S. Food and Drug Administration. Post-processing of the solutions was performed using OpenFOAM and the open-source software ParaView (Kitware, Inc., Clifton Park, NY), the latter of which was also used to visualize the results.

### Solution Verification

In this study, we use a two-pronged approach to solution verification: (i) qualitative evaluation of the influence of mesh resolution on the prediction of local solution field variables, and (ii) quantitative evaluation of the numerical uncertainty of integrated scalar quantities of interest. Specifically, we conduct a mesh refinement study at the highest flow rate (exercise) condition using the series of eight meshes described in Section “Computational Mesh”. To quantitatively estimate the numerical uncertainty, we calculate the grid convergence index (GCI) using generalized Richardson extrapolation.<sup>22,27,28</sup> Originally established by Roache,<sup>26</sup> the GCI represents a conservative estimation

or “banding” of the numerical uncertainty present in the computed solution due to discretization error.<sup>28</sup>

Briefly, the GCI is calculated using CFD solutions computed on a series of three consistently refined meshes, which are collectively termed a mesh “triplet”.<sup>28</sup> Here, we denote the three meshes as coarse, medium, and fine. Ideally, the meshes should be consistently and uniformly refined using the same mesh refinement ratio,  $r$ , defined as

$$r \approx \left( \frac{N_{medium}}{N_{coarse}} \right)^{1/3} \approx \left( \frac{N_{fine}}{N_{medium}} \right)^{1/3} \quad (4)$$

for unstructured meshes, where  $N$  is the number of computational cells in each mesh.<sup>28</sup> Computed solutions of the scalar quantity of interest,  $f$ , are used to calculate the observed order of convergence,  $p$ , via:

$$p = \frac{\ln\left(\frac{f_{coarse} - f_{medium}}{f_{medium} - f_{fine}}\right)}{\ln(r)} \quad (5)$$

where  $f_{coarse}$ ,  $f_{medium}$ , and  $f_{fine}$  are the coarse, medium, and fine mesh solutions, respectively. An estimate of the fractional error in the fine mesh solution may then be calculated as:

$$E_{fine} = \frac{(f_{medium} - f_{fine})}{f_{fine}} \cdot \frac{1}{r^p - 1}. \quad (6)$$

Finally, the GCI of the fine mesh solution is calculated as:

$$GCI_{fine} = F_s |E_{fine}| \quad (7)$$

where  $F_s$  is a factor of safety that is used to ensure that the resultant GCI represents a conservative estimate of the numerical uncertainty.

In the present study, we calculate multiple values of GCI using six sets of mesh triplets from our series of eight CFD meshes (see Section “Computational Mesh”). Specifically, the mesh triplets include Meshes 1–3, 2–4, 3–5, 4–6, 5–7, and 6–8. Since the eight meshes were created with each successive (finer) mesh having approximately twice the number of computational cells as the preceding (coarser) mesh, the refinement ratio is  $r \approx 1.26$  between each successive mesh pair. Additionally, because we use mesh triplets to calculate the observed order of convergence *via* Eq. (5), as recommended by Roache<sup>28</sup> we use a factor of safety,  $F_s$ , of 1.25 when calculating values of GCI (Eq. 7).

### Helicity

In this work, we are most interested in the fluid dynamics in the IVC with particular emphasis on flow patterns that influence embolus transport. As shown by Aycock *et al.*,<sup>5</sup> swirl and mixing in the IVC impart

cross-stream forces on emboli that can significantly affect their trajectory. Helicity is a parameter that may be used to quantify the amount of such swirl and mixing (e.g., see Refs. 9, 12, 18, 35, 40). Indeed, as demonstrated by Mukherjee *et al.*,<sup>19</sup> helicity is an excellent fluid dynamic indicator of local embolus particle transport in cardiovascular flows.

The term “helicity” was first proposed by Moffatt.<sup>17</sup> Mathematically, it is defined as<sup>16</sup>:

$$H = \int_V \mathbf{u} \cdot \boldsymbol{\omega} dV \quad (8)$$

where  $\boldsymbol{\omega} = \nabla \times \mathbf{u}$  is the vorticity vector and the integration is performed over a bounded or unbounded domain of volume  $V$ . The integrand of Eq. (8) represents the helicity per unit volume and is referred to as the helicity density,  $h = \mathbf{u} \cdot \boldsymbol{\omega}$ . A related quantity known as the normalized helicity density,<sup>31,40</sup> or the local normalized helicity ( $LNH$ ),<sup>12,18</sup> is defined as

$$LNH = \frac{\mathbf{u} \cdot \boldsymbol{\omega}}{|\mathbf{u}| |\boldsymbol{\omega}|}. \quad (9)$$

Because  $LNH$  is the helicity density normalized by the product of velocity and vorticity magnitude, it has a range of  $[-1, 1]$ .

Physically, helicity may be thought of as the amount of swirl or helical motion that a flow experiences either locally ( $LNH$ ) or globally within a domain ( $H$ ). The signed value of  $LNH$ , which is determined by the term  $\mathbf{u} \cdot \boldsymbol{\omega}$ , has particular significance as it designates the “screw” of the helical rotation.<sup>17</sup> A positive value of  $LNH$  indicates that the flow is swirling in a clockwise direction when looking downstream. Conversely, a negative value of  $LNH$  indicates that the flow is swirling in a counter-clockwise direction. The strength of the local helical motion is quantified by the magnitude of  $LNH$ : a value of zero signifies no local helicity, and values close to either end of the range ( $-1$  or  $1$ ) indicate appreciable local helical flow.

To quantify the amount of swirl and mixing in the IVC, we calculate both local and global helicity parameters. We use  $LNH$  (Eq. 9) to characterize the local distribution of helicity. To characterize a global measure of helicity in the domain, we use the volume-averaged helicity intensity of Gallo *et al.*<sup>12</sup> defined as

$$\overline{HI} = \frac{1}{V} \int_V |\mathbf{u} \cdot \boldsymbol{\omega}| dV. \quad (10)$$

Compared with helicity (Eq. 8), the use of  $\overline{HI}$  has two advantages in the present context. First, because it is defined in terms of the absolute value of the helicity density,  $\overline{HI}$  quantifies the total amount of helicity in the domain, irrespective of rotational direction.<sup>12</sup> This

is not true of global helicity parameters based on the signed value of helicity density (e.g.,  $H$ ) that are zero when integrated over a domain containing symmetric counter-rotating vortices.<sup>12</sup> Finally, we define  $\overline{HI}$  as a volumetric average to make it insensitive to the size of the flow domain. Thus, as defined,  $\overline{HI}$  represents the average magnitude of helicity density present in the flow domain.

## RESULTS

In this study, we verify and validate CFD simulations of flow patterns in a patient-averaged anatomical model of the IVC. In Section “[Solution Verification: Mesh Refinement Study](#)”, we present the results of a mesh refinement study that we performed to ensure that the results are mesh-convergent and to quantify the numerical uncertainty present in the CFD predictions. To validate the CFD results, in Section “[Validation: Comparison with PIV](#)” we then compare CFD predictions of the flow field with PIV data in the same model.<sup>11</sup>

### *Solution Verification: Mesh Refinement Study*

We performed a mesh refinement study at the highest flow rate condition (exercise) using the eight meshes listed in Table 2. The exercise flow rate was chosen because it has the largest Reynolds number (about 1500 in the infrarenal IVC), which indicates more appreciable inertial effects and a greater degree of mixing compared with the resting flow rate condition. A finer mesh is generally required to resolve higher Reynolds number flows with more mixing. Thus, performing the mesh refinement study at exercise conditions ensures that the estimated discretization error (i.e., values of GCI) will also be conservative for resting conditions, where less complex flow patterns and mixing are expected.

As previously mentioned in Section “[Solution Verification](#)”, we use a two-pronged approach to solution verification: (i) qualitative evaluation of the influence of mesh resolution on the prediction of the local solution field, and (ii) quantitative evaluation of the numerical uncertainty of scalar quantities of interest. In the present study, we are most interested in the fluid dynamics in the IVC that influence embolus transport and IVC filter embolus trapping. Accordingly, we restrict our analyses to the comparison of velocity and the amount of swirl and mixing. Specifically, we compare qualitative distributions of the velocity field that elucidate the gross flow patterns in the IVC and detailed secondary flow patterns in the infrarenal sec-



tion. Quantitatively, we consider the numerical uncertainty and mesh convergence of maximum velocity magnitude in the domain and the amount of secondary flow in the infrarenal IVC, as quantified by the area-averaged transverse velocity magnitude. To further compare the amount of mixing, we examine qualitative distributions of the local normalized helicity ( $LNH$ ) (Eq. 9). Finally, we evaluate the mesh convergence of the volume-averaged helicity intensity ( $\overline{HI}$ ) (Eq. 10) and the numerical uncertainty present in the CFD solutions by calculating values of GCI (see Section “[Solution Verification](#)”).

### Velocity Distribution

Comparing the gross flow patterns in the patient-averaged IVC model at exercise flow conditions (Fig. 4), the results obtained using each of the meshes are virtually indistinguishable from one another. In each case, the flow enters the model as fully developed at each iliac inlet and proceeds downstream, undisturbed until reaching the confluence of the iliac veins. At the iliac vein confluence, the parabolic profile from each vein is vectored toward the center of the infrarenal IVC, where the flow streams merge and form a high-velocity region in the center of the IVC lumen with a pair of counter-rotating vortices on either side (see Fig. 4). This flow pattern causes significant swirl and mixing within the infrarenal IVC.

Comparing detailed flow patterns within the infrarenal IVC (Fig. 5), there is a subtle qualitative difference between the coarsest and finer CFD mesh solutions. Transverse velocity vectors illustrate the same gross secondary flow pattern in each case. However, the counter-rotating vortices are clearly not as well resolved using the coarsest mesh (Mesh 1) compared with the finer meshes. Close inspection of the contours of velocity magnitude for Meshes 5 and 7 reveals no discernible qualitative difference in the computed velocity distribution in the infrarenal IVC using the more refined CFD meshes.

### Helicity Distribution

To investigate the influence of mesh resolution on the qualitative distribution of swirl and mixing in the infrarenal IVC, we compare predictions of the local normalized helicity ( $LNH$ ) (Fig. 6). Here, we see a much more noticeable qualitative effect of mesh resolution. This is due to the fact that calculating  $LNH$  (Eq. 9) requires the computation of vorticity and, thus, the local velocity gradient. Compared to predictions of local velocity, velocity gradients tend to be more sen-

sitive to mesh resolution because mesh spacing is in the denominator of the gradient calculation.

The mesh sensitivity of the  $LNH$  predictions is particularly evident by comparing the results for Meshes 1 and 7 (Fig. 6). The  $LNH$  field is not nearly as well resolved using the coarsest mesh (Mesh 1) compared with the finer mesh (Mesh 7). This is especially apparent by observing the fine-scale structure in the  $LNH$  field for Mesh 7 and the lack thereof for Mesh 1. Comparing Meshes 5 and 7, there is no discernible qualitative difference in the predicted  $LNH$  distribution in the infrarenal IVC using the more refined CFD meshes.

### Quantitative Mesh Convergence

To quantitatively evaluate mesh convergence, we consider three scalar quantities of interest: (i) maximum velocity magnitude in the domain, (ii) the area-averaged transverse velocity magnitude at a cross-section in the infrarenal IVC, and (iii) the volume-averaged helicity intensity,  $\overline{HI}$  (Eq. 10). The area-averaged transverse velocity magnitude is defined as:

$$\overline{|\mathbf{u}_{tr}|} = \frac{1}{A} \int_A |\mathbf{u} - (\mathbf{u} \cdot \mathbf{n})\mathbf{n}| dA \quad (11)$$

where the integration is performed over a transverse cross-section. Here, we use the same cross-section shown in Figs. 3, 5, and 6, which is located approximately 10 cm downstream of the confluence of the iliac veins. The quantity  $\overline{|\mathbf{u}_{tr}|}$  was chosen, as it represents a local integrated measure of secondary flow. For each scalar quantity of interest, using Richardson extrapolation (see Section “[Solution Verification](#)”), we calculate values of the observed order of convergence and GCI (Table 3).

As shown in Fig. 7, each of the scalar quantities of interest converge monotonically with mesh refinement toward the exact solution that would be reached in the limit of infinite mesh resolution. In general, as we refine the mesh we resolve a higher maximum velocity and more swirl and mixing in the IVC. The maximum velocity magnitude in the domain converges more quickly than either  $\overline{|\mathbf{u}_{tr}|}$  or  $\overline{HI}$ . The corresponding values of GCI are also much lower for  $|\mathbf{u}|_{max}$  than either  $\overline{|\mathbf{u}_{tr}|}$  or  $\overline{HI}$  for each mesh, with an estimated numerical uncertainty in  $|\mathbf{u}|_{max}$  ranging from about 1% for Meshes 3 and 4 to 0.05% for Mesh 8. Interestingly, the mesh convergence of  $\overline{|\mathbf{u}_{tr}|}$  is comparable to  $\overline{HI}$ , with GCI values ranging from on the order of 15% for Mesh 3 to less than 1% for Mesh 8 (Table 3).



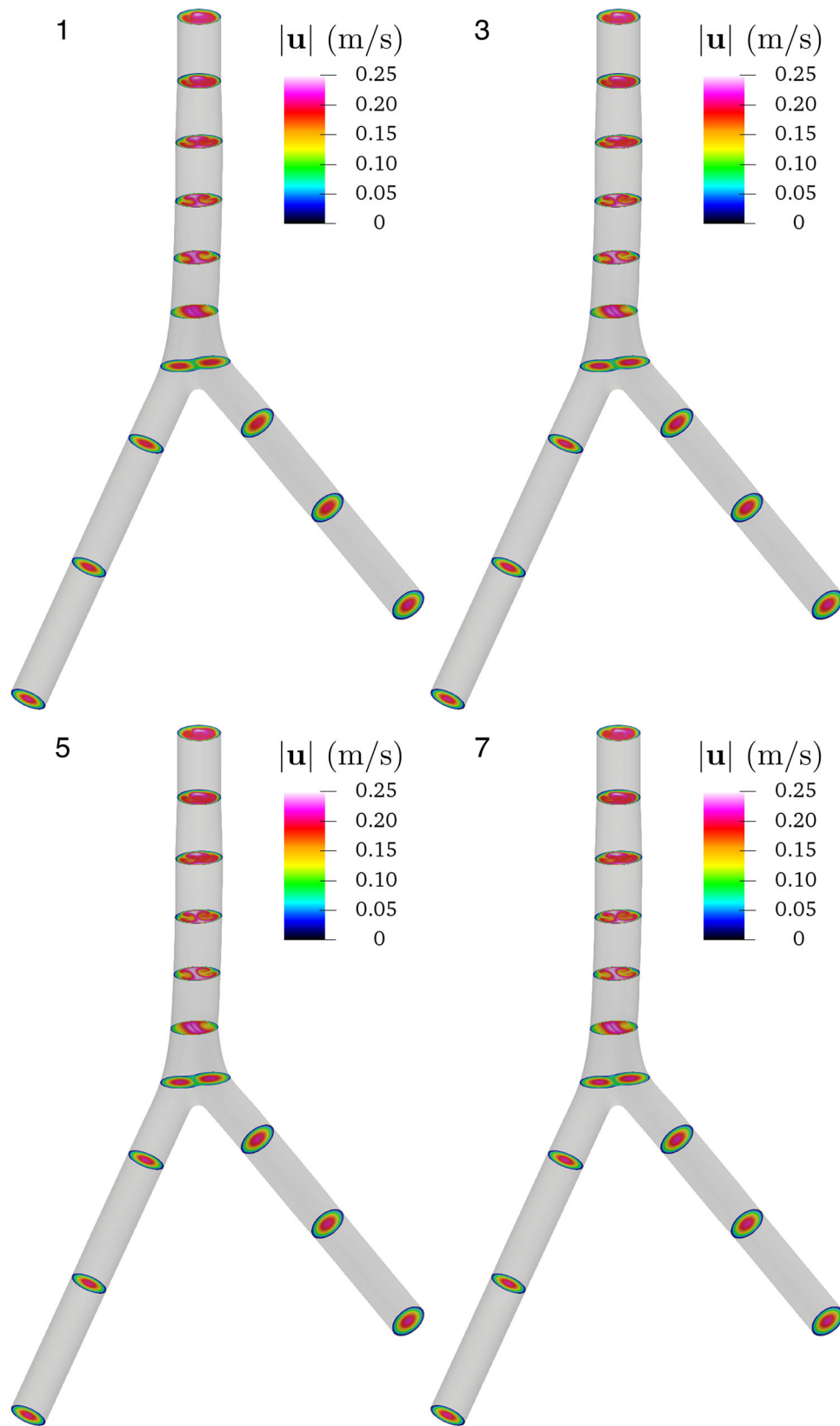
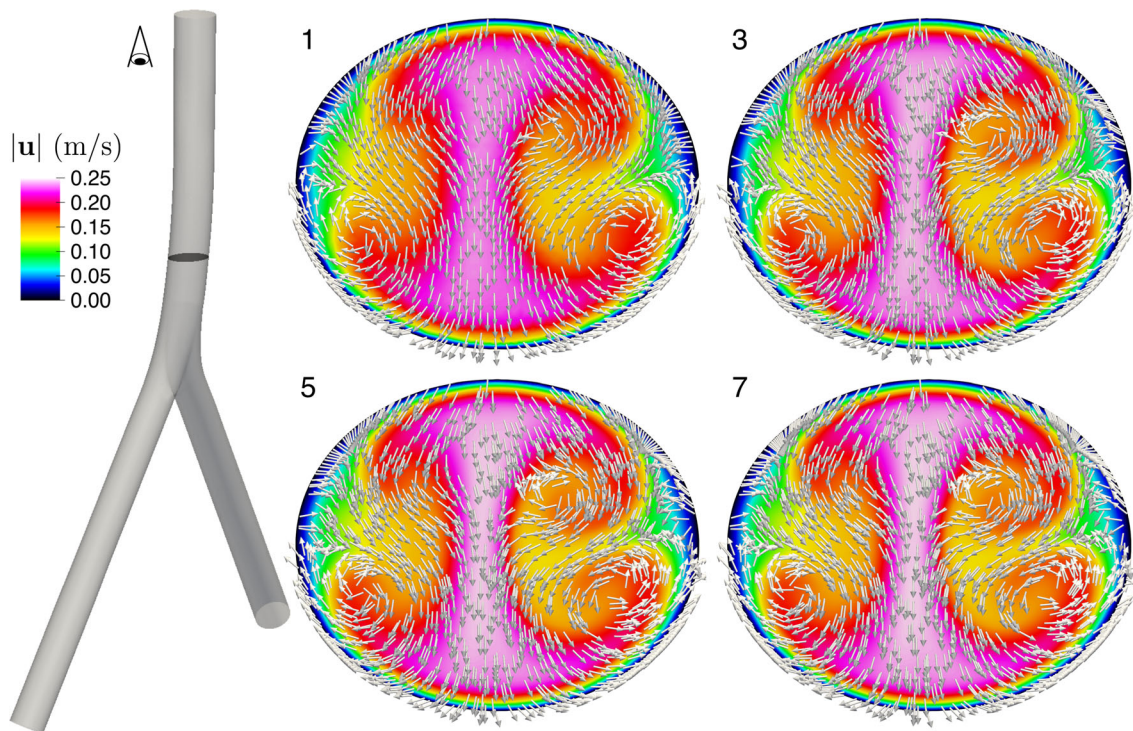


FIGURE 4. Comparison of gross flow patterns in the patient-averaged IVC for the exercise flow condition obtained using Meshes 1, 3, 5, and 7 (see Table 2 and Fig. 3).



**FIGURE 5.** Contours of velocity magnitude with transverse velocity vectors illustrating secondary flow patterns in the infrarenal IVC for the exercise flow condition obtained using Meshes 1, 3, 5, and 7 (see Table 2). The location of the transverse cross-section shown for each mesh is illustrated in the inset. The cross-section is located approximately 10 cm downstream of the confluence of the iliac veins and is the same as that shown in Fig. 3. Each cross-section is viewed from a superior perspective (i.e., looking upstream).

#### *Validation: Comparison with PIV*

Given the results of the foregoing mesh refinement study, we chose to use Mesh 6 for comparison with the experimental data of Gallagher *et al.*<sup>11</sup> that was acquired in the same patient-averaged IVC model. This is because Mesh 6 was shown to resolve the qualitative distributions of velocity and helicity in the IVC at the highest flow rate condition (exercise). Additionally, we demonstrated that Mesh 6 yields mesh-converged quantitative predictions of  $|\mathbf{u}|_{max}$ ,  $|\overline{\mathbf{u}_{tr}}|$ , and  $\overline{HI}$  in the patient-averaged IVC, with estimated values of numerical uncertainty of 0.24, 2.15, and 2.68%, respectively.

Here, we perform a validation study by comparing our Mesh 6 CFD results with the PIV data of Gallagher *et al.*<sup>11</sup> Specifically, we compare the velocity field in two planes (coronal and sagittal) within the infrarenal IVC at two flow rates corresponding to rest and exercise conditions. To enable a consistent comparison, we manually aligned the PIV data with the IVC geometry in the coordinate system of the CFD data. The CFD data were then extracted in the same planes as the PIV data. The two-dimensional velocity magnitude,  $|u_{2D}|$ , was then calculated for both data sets in each plane. Contours of  $|u_{2D}|$  were then plotted on

the same scale for the rest and exercise flow rate conditions for each plane and compared.

As described in Section “[Verification and Validation Terminology](#)”, the comparison of simulation results with experiments can take varying forms depending on the rigor of the comparison. Here, we compare qualitative distributions of the velocity field in each plane at rest (Section “[Velocity Distribution at Rest Conditions](#)”) and exercise (Section “[Velocity Distribution at Exercise Conditions](#)”) conditions to validate CFD predictions of the flow patterns in the infrarenal IVC. A more rigorous comparison of the velocity field is then performed by calculating a global validation comparison error to quantify the average relative percent difference between CFD and PIV (Section “[Quantitative Comparison](#)”). Given that there is some uncertainty associated with the manual alignment of the PIV data with the IVC geometry used for CFD, we next analyze the sensitivity of the qualitative and quantitative validation results to minor variations in the alignment of the PIV plane (Section “[Sensitivity to PIV Plane Thickness and Location](#)”). Finally, we perform a sensitivity study to investigate the influence of input uncertainty on the CFD solution and the PIV-CFD comparison (Section “[Sensitivity to Input Uncertainty](#)”).

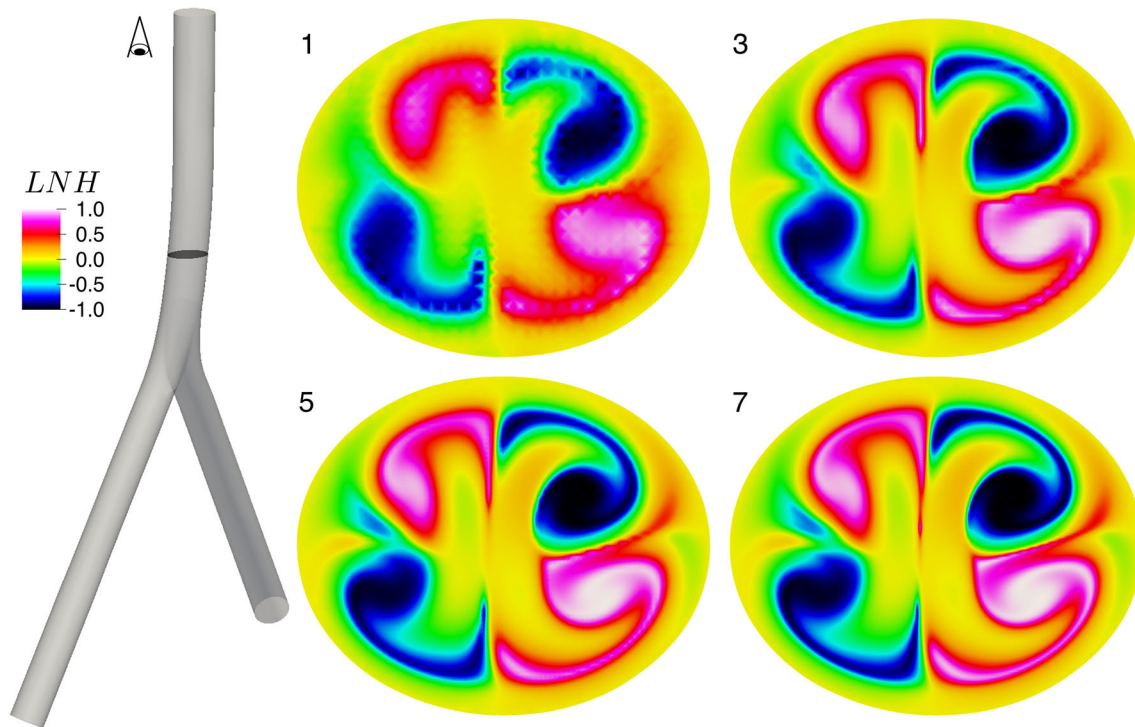


**FIGURE 6.** Contours of the local normalized helicity ( $LNH$ ) in the infrarenal IVC for the exercise flow condition obtained using Meshes 1, 3, 5, and 7 (see Table 2). The location of the transverse cross-section shown for each mesh is illustrated in the inset. The cross-section is located approximately 10 cm downstream of the confluence of the iliac veins and is the same as that shown in Figs. 3 and 5. Each cross-section is viewed from a superior perspective (i.e., looking upstream).

#### *Velocity Distribution at Rest Conditions*

At the resting flow rate condition, a roughly parabolic velocity distribution is observed in the coronal plane of the infrarenal IVC (Fig. 8). A more blunt velocity distribution exists in the sagittal plane. Aside from a slight difference in the velocity magnitude in the sagittal plane, the qualitative comparison of the CFD prediction and the PIV measurements is excellent.

#### *Velocity Distribution at Exercise Conditions*

At the exercise flow rate condition, there is a sharp increase in the velocity magnitude with a peak near the center of the IVC lumen in the coronal plane (Fig. 9). Considering the three-dimensional velocity field shown in Fig. 5, this peak velocity corresponds to the high-velocity region that exists between the two pairs of counter-rotating vortices that develop downstream of the iliac vein confluence. In the sagittal plane, the velocity distribution is fairly uniform, except within the central-superior region, where a slight velocity deficit is observed (Fig. 9). From the three-dimensional flow field (Fig. 5), the sagittal plane appears to be within the aforementioned high-velocity region in the center of the IVC lumen where a fairly uniform, high velocity exists. The plane appears to cut through the edge of

one of the counter-rotating vortex pairs where there is a lower velocity, which explains the slight velocity deficit observed in both the PIV and CFD data.

Overall, the qualitative comparison of the CFD prediction and the PIV measurements is excellent in both planes. In the coronal plane, the CFD simulation accurately predicts the magnitude and approximate location of the high-velocity region in the center of the IVC lumen. In the sagittal plane, the simulation predicts the occurrence of uniform, high-speed flow with a slight velocity deficit that appears to correspond with the edge of one of the counter-rotating vortex pairs. Taken together, the CFD results and PIV measurements show excellent qualitative agreement, demonstrating that the CFD simulation predicts the same flow speeds and detailed flow patterns in the infrarenal IVC at exercise conditions as observed in the experiments.

#### *Quantitative Comparison*

To quantitatively compare the CFD predictions and PIV measurements we calculate the global relative comparison error for both planes (coronal and sagittal) at each condition (rest and exercise). The global relative comparison error,  $E$ , is defined as



**TABLE 3. Quantitative evaluation of the numerical uncertainty present in the CFD predictions of maximum velocity magnitude,  $|u|_{max}$ , area-averaged transverse velocity magnitude,  $|u_{tr}|$ , and volume-averaged helicity intensity,  $\overline{HI}$ , in the patent-averaged IVC model for the exercise flow condition obtained using Meshes 1–8.**

Mesh	Maximum velocity			Transverse velocity			Helicity		
	$ u _{max}$ (m/s)	$p$	$GCI$ (%)	$ u_{tr} $ (m/s)	$p$	$GCI$ (%)	$\overline{HI}$ (m/s <sup>2</sup> )	$p$	$GCI$ (%)
1	0.24503	–	–	0.01596	–	–	0.38173	–	–
2	0.24801	–	–	0.01708	–	–	0.40561	–	–
3	0.24972	2.39	1.17	0.01786	1.51	13.19	0.42360	1.23	16.16
4	0.25095	1.44	1.56	0.01838	1.81	6.81	0.43629	1.51	8.73
5	0.25165	2.49	0.44	0.01871	1.99	3.76	0.44476	1.75	4.78
6	0.25203	2.52	0.24	0.01891	2.09	2.15	0.45019	1.93	2.68
7	0.25223	2.95	0.10	0.01904	2.14	1.27	0.45351	2.12	1.45
8	0.25233	3.05	0.05	0.01911	2.22	0.72	0.45549	2.24	0.80

$|u_{tr}|$  is calculated at the cross-section shown in Figs. 3, 5, and 6, which is located approximately 10 cm downstream of the confluence of the iliac veins. Here,  $p$  is the observed order of convergence and  $GCI$  is the grid convergence index (see Section “Solution Verification”).

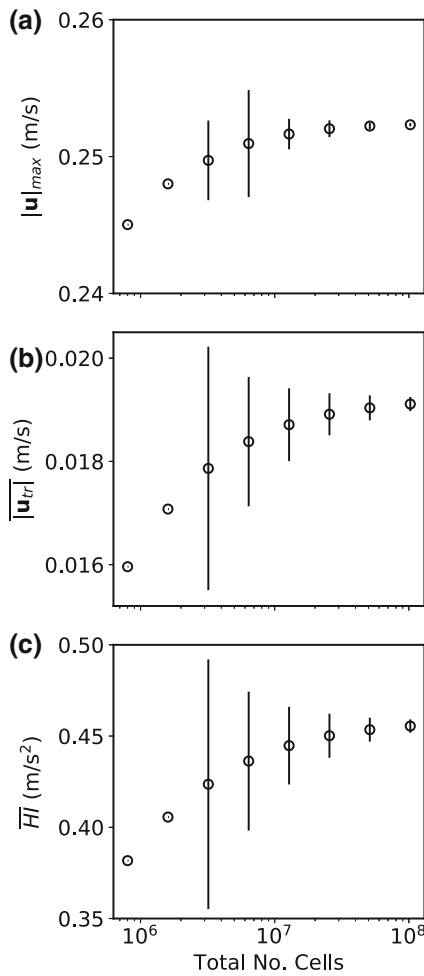


**FIGURE 7. Quantitative comparison of the (a) maximum velocity magnitude,  $|u|_{max}$ , (b) area-averaged transverse velocity magnitude,  $|u_{tr}|$ , and (c) volume-averaged helicity intensity,  $\overline{HI}$ , in the patent-averaged IVC model for the exercise flow condition obtained using Meshes 1–8.  $|u_{tr}|$  is calculated at the cross-section shown in Figs. 3, 5, and 6, which is located approximately 10 cm downstream of the confluence of the iliac veins. Error bars are included for Meshes 3–8 that represent the numerical uncertainty of each CFD prediction, quantified by the grid convergence index (Table 3).**

$$E(\%) = \frac{1}{n} \sum_{i=1}^n \left| \frac{|u_{2d}|_{PIV,i} - |u_{2d}|_{CFD,i}}{|u_{2d}|_{PIV}} \right| \times 100 \quad (12)$$

where  $|u_{2d}|_{PIV,i}$  is the two-dimensional velocity magnitude at each spatial location comprising the PIV velocity contour data,  $|u_{2d}|_{CFD,i}$  is the corresponding CFD prediction at the same spatial location, and  $|u_{2d}|_{PIV}$  is the average two-dimensional velocity magnitude measured with PIV in each plane. Mathematically,  $E$  represents the average relative in-plane discrepancy (or percent difference) between CFD and PIV.

As summarized in Table 4, the comparison error is 3.03 and 6.77% at the resting flow rate condition in the coronal and sagittal planes, respectively. At the exercise flow rate condition, the comparison error is likewise in the same range (5.56%) in the sagittal plane. In the coronal plane, however, the comparison error at exercise conditions is larger (10.98%).

#### Sensitivity to PIV Plane Thickness and Location

The largest comparison error between CFD and PIV (10.98%) is for the coronal plane at exercise flow rate conditions (Table 4). From Fig. 5, we note that the coronal plane approximately bisects both pairs of counter-rotating vortices that are present at exercise conditions in the infrarenal IVC. Because of this, there are large out-of-plane velocity gradients normal to the coronal plane that could potentially influence the comparison of the PIV and CFD results in two ways.

First, the laser sheet used in the PIV experiments had a reported thickness of 750  $\mu\text{m}$ .<sup>11</sup> Physically, this means that the PIV data represent an integrated average velocity measurement within the swept volume of the laser sheet. In comparing with CFD, however, we extracted velocity data from the CFD predictions

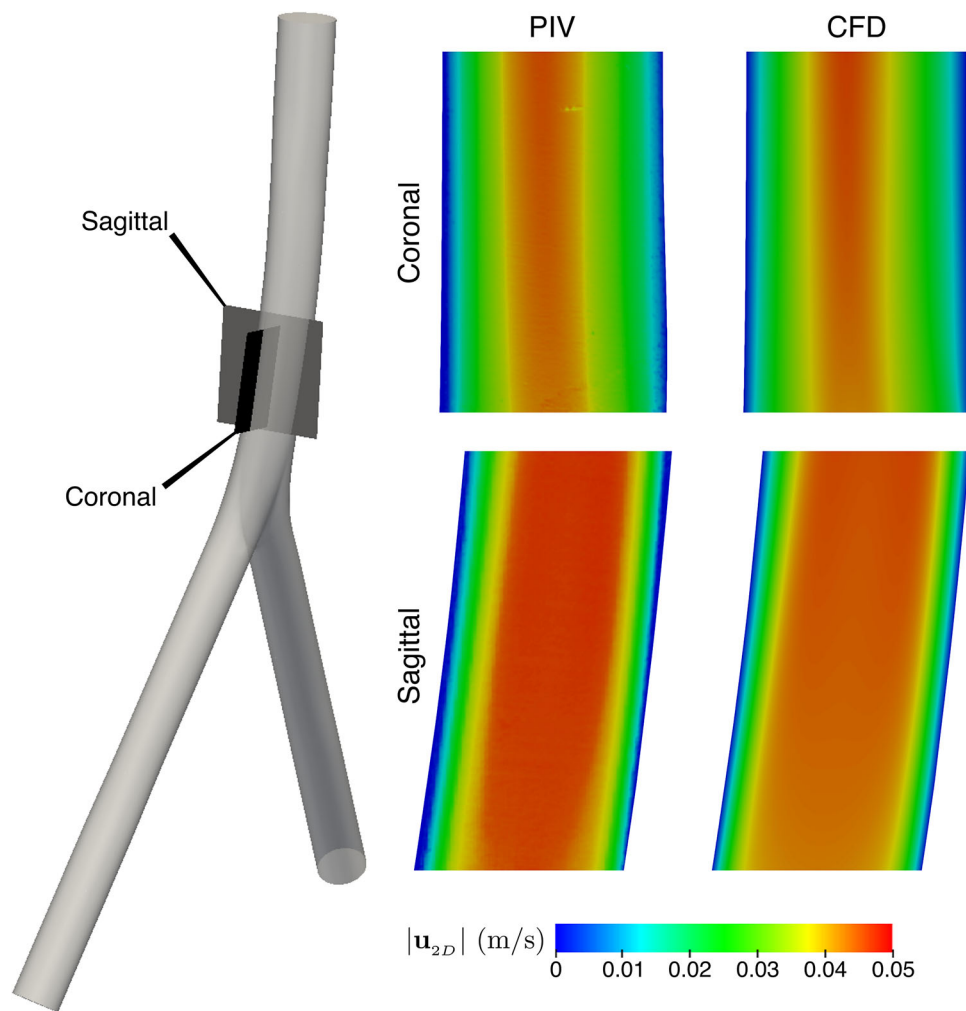


**FIGURE 8.** Comparison of PIV measurements and CFD predictions of the velocity field in two planes (coronal and sagittal) within the infrarenal IVC at resting flow rate conditions. In each case, contours of the two-dimensional velocity magnitude,  $|u_{2D}|$ , are shown in the PIV plane.

within the nominal coronal plane, which is infinitely thin. Thus, there is some uncertainty associated with comparing PIV measurements acquired in a laser sheet of finite thickness with CFD results extracted in a plane.

Second, there is some inherent uncertainty associated with our manual alignment of the PIV data with the IVC geometry used for CFD. While this alignment allowed for a consistent comparison of PIV measurements and CFD results, due to the large out-of-plane velocity gradients normal to the coronal plane at exercise conditions, small variations in the alignment could potentially influence the PIV-CFD comparison.

To investigate the influence of both uncertainties (due to PIV laser sheet thickness and alignment location), we performed a sensitivity study using the CFD results from Mesh 6. Specifically, we offset the nominal coronal plane by  $\pm 1$  mm in the normal direction and

extracted results from the CFD solution to examine the influence of such small variations on the quantitative comparison of the PIV and CFD results. As summarized in Table 5, small variations of  $\pm 1$  mm in the coronal plane location lead to variations in the relative comparison error of between 1.6 and 3.2%. However, the comparison error is still  $\sim 10\%$ , indicating that the discrepancy between CFD and PIV in the coronal plane at exercise conditions is not solely due to the influence of the PIV laser sheet thickness or uncertainty associated with the manual alignment of the data.

#### *Sensitivity to Input Uncertainty*

To further explore possible reasons for the discrepancy between the PIV measurements and CFD results, we consider the influence of input uncertainty.

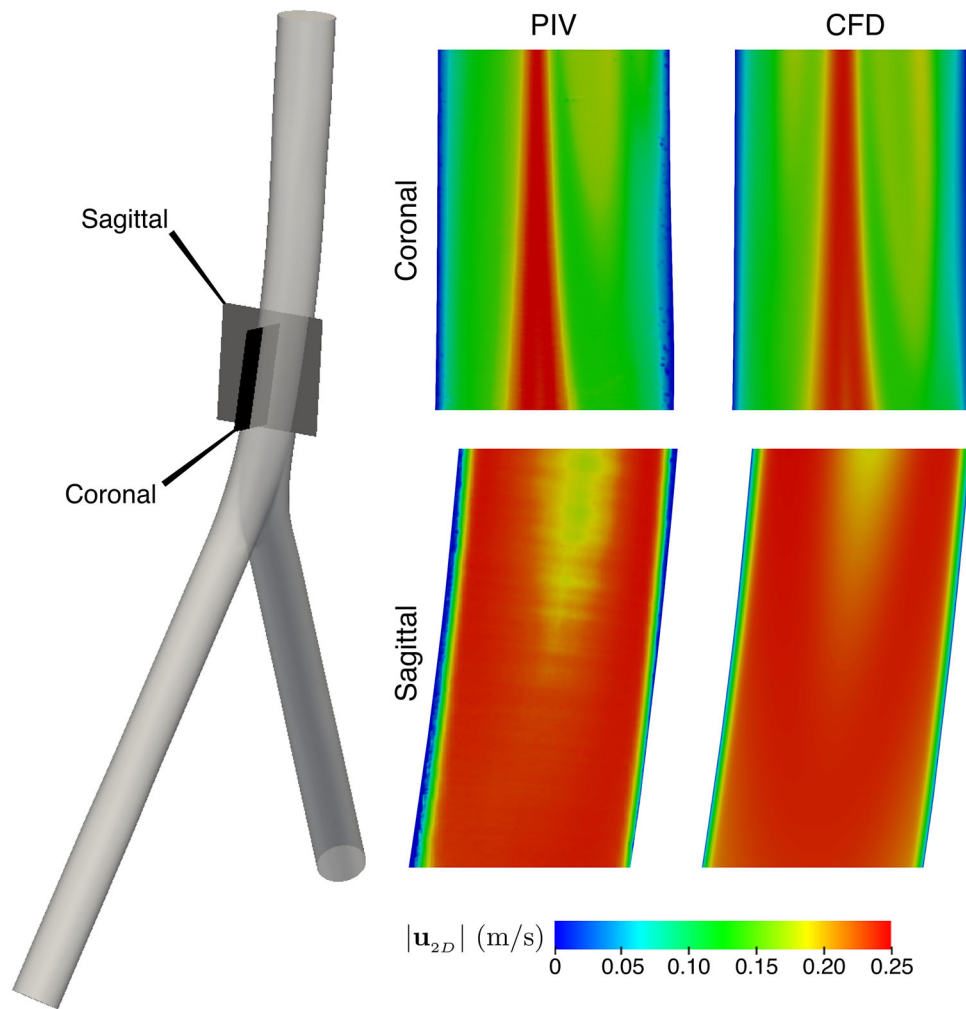


FIGURE 9. Comparison of PIV measurements and CFD predictions of the velocity field in two planes (coronal and sagittal) within the infrarenal IVC at exercise flow rate conditions. In each case, contours of the two-dimensional velocity magnitude,  $|u_{2D}|$ , are shown in the PIV plane.

TABLE 4. Global relative comparison error (Eq. 12) between CFD and PIV in the coronal and sagittal planes at rest and exercise conditions.

Plane	Condition	
	Rest (%)	Exercise (%)
Coronal	3.03	10.98
Sagittal	6.77	5.56

The two primary input parameters that influence the fluid dynamics include: (i) the kinematic viscosity of the fluid, and (ii) the inlet flow rate to each iliac vein. To investigate the influence of each input parameter on the CFD solution and the PIV-CFD comparison, we performed a sensitivity study at exercise flow rate conditions using Mesh 6.

TABLE 5. Sensitivity of the global relative comparison error (Eq. 12) between CFD and PIV in the coronal plane at exercise conditions to small variations in the location of the coronal plane.

Plane location	$E$ (%)
Nominal	10.98
Nominal + 1 mm	14.13
Nominal - 1 mm	9.36

The nominal location corresponds to the location of the PIV plane after it was manually aligned with the IVC geometry used for CFD. To investigate the sensitivity of the comparison error to small variations in the coronal plane location, the nominal coronal plane was offset in the normal direction by  $\pm 1$  mm.

We explored the sensitivity of the CFD solution to changes in the kinematic viscosity,  $\nu$ , by performing two additional simulations using a viscosity of  $3.12 \times 10^{-6}$  and  $2.92 \times 10^{-6}$   $\text{m}^2/\text{s}$ . These values correspond to



**TABLE 6. Sensitivity of the global relative comparison error (Eq. 12) between CFD and PIV in the coronal plane at exercise conditions to uncertainty in the input parameters.**

Input parameter	Value	$E$ (%)
Nominal		10.98
$\nu$ (m <sup>2</sup> /s)	$3.12 \times 10^{-6}$ (+3.3%)	10.82
$\nu$ (m <sup>2</sup> /s)	$2.92 \times 10^{-6}$ (-3.3%)	11.16
$Q_{LI}$ (L/min)	2.7 (-10%)	14.29
$Q_{RI}$ (L/min)	3.3 (+10%)	
$Q_{LI}$ (L/min)	2.85 (-5%)	12.38
$Q_{RI}$ (L/min)	3.15 (+5%)	
$Q_{LI}$ (L/min)	3.15 (+5%)	9.69
$Q_{RI}$ (L/min)	2.85 (-5%)	
$Q_{LI}$ (L/min)	3.3 (+10%)	8.62
$Q_{RI}$ (L/min)	2.7 (-10%)	

Here,  $\nu$  is the kinematic viscosity of the fluid,  $Q_{LI}$  is the volumetric flow rate in the left iliac vein, and  $Q_{RI}$  is the right iliac flow rate.

changes in the viscosity associated with the reported uncertainty and variability of the fluid temperature measurements of Gallagher *et al.*<sup>11</sup> Specifically, the reported accuracy of the fluid temperature measurements is in the  $\pm 1$ –2% range, whereas the reported variability in the fluid temperature during the experiments is about 4%. Thus, we calculated values of viscosity (from Eq. 1 in Gallagher *et al.*<sup>11</sup>) that correspond to  $\pm 4\%$  variability in the nominal fluid temperature (26.6 °C). This yields a variability of  $\pm 3.3\%$  in kinematic viscosity.

As shown in Fig. 10, the CFD solution is fairly insensitive to uncertainty in the kinematic viscosity. Close inspection of the predicted flow patterns in the CFD transverse cross-sections in Figs. 10a, 10b, and 10c reveals that there is no noticeable change in the location of the high velocity region in the center of the IVC lumen or in the strength and location of the counter-rotating vortices. Quantitatively, such variability in  $\nu$  had a minor influence on the global comparison error between CFD and PIV in the coronal plane, yielding a variability in  $E$  of about  $\pm 0.2\%$  (Table 6).

We next explore the sensitivity of the CFD solution to changes in the volumetric flow rate of each iliac vein. Gallagher *et al.*<sup>11</sup> report a measurement accuracy of the inlet flow rate of  $\pm 10\%$  and variability in the measured flow rate during the experiments of about 0.3%. Thus, to investigate the sensitivity of the results to uncertainty in the inlet flow rate, we performed four additional CFD simulations and varied the nominal inlet flow rate by  $\pm 5\%$  and  $\pm 10\%$  for both the left and right iliacs.

As shown in Fig. 10, the CFD solution is sensitive to changes in the inlet flow rate of each iliac. In general, as the inlet flow rate to the left iliac increases the

high velocity region in the center of the IVC lumen shifts to the right, and *vice versa*. Higher values of the left iliac inlet flow rate and lower right iliac flow rates yield CFD predictions of the infrarenal IVC flow patterns that better align with the observed PIV flow patterns in the coronal plane. This is apparent from Figs. 10a and 10e, which reveal that the predicted IVC flow patterns from the nominal CFD simulation are slightly offset from the PIV measurements. Specifically, the central high velocity region is slightly shifted to the left for the nominal CFD compared to PIV, as illustrated by the inset in Fig. 10a. In Fig. 10e we see that, as the left iliac flow rate increases and the right iliac flow rate decreases, the central high velocity region shifts to the right and better aligns with the measured velocity distribution from PIV.

The observed sensitivity of the PIV-CFD comparison to uncertainty in the inlet flow rate is quantitatively confirmed by the corresponding values of the global comparison error between CFD and PIV in the coronal plane (Table 6). Varying the inlet flow rate by  $\pm 10\%$  for both iliacs yields values of  $E$  that vary between 14.29 and 8.62%, with the best comparison corresponding to a higher left iliac flow rate and a lower right iliac flow rate. Thus, the quantitative discrepancy between CFD and PIV in the coronal plane at exercise conditions reported in Section “Quantitative Comparison” is also likely attributable to uncertainty in the input parameters—particularly, values of the inlet flow rate to each iliac vein.

## DISCUSSION

In this study, we perform CFD simulations of flow in a patient-averaged anatomical model of the inferior vena cava (IVC) at rest and exercise conditions. At rest conditions, the flow is relatively simple, with flow from both iliacs merging to form a quasi-parabolic flow profile in the IVC with little secondary flow and mixing. At exercise conditions, however, the flow patterns are much more complex, as flow from the iliacs merge and interact to form a pair of counter-rotating vortices with a high-velocity region in the center of the IVC lumen. These flow patterns are similar to those reported by Ren *et al.*<sup>24</sup> at comparable flow rates in the original model of Rahbar *et al.*<sup>23</sup> upon which the present model is based.

Compared with the experiments of Gallagher *et al.*,<sup>11</sup> the qualitative agreement between the computed flow patterns and PIV measurements is excellent at both flow conditions. At the resting flow condition, the CFD results closely match the PIV data, aside from a slight difference in the velocity magnitude in the sagittal plane. At the exercise flow rate, the CFD

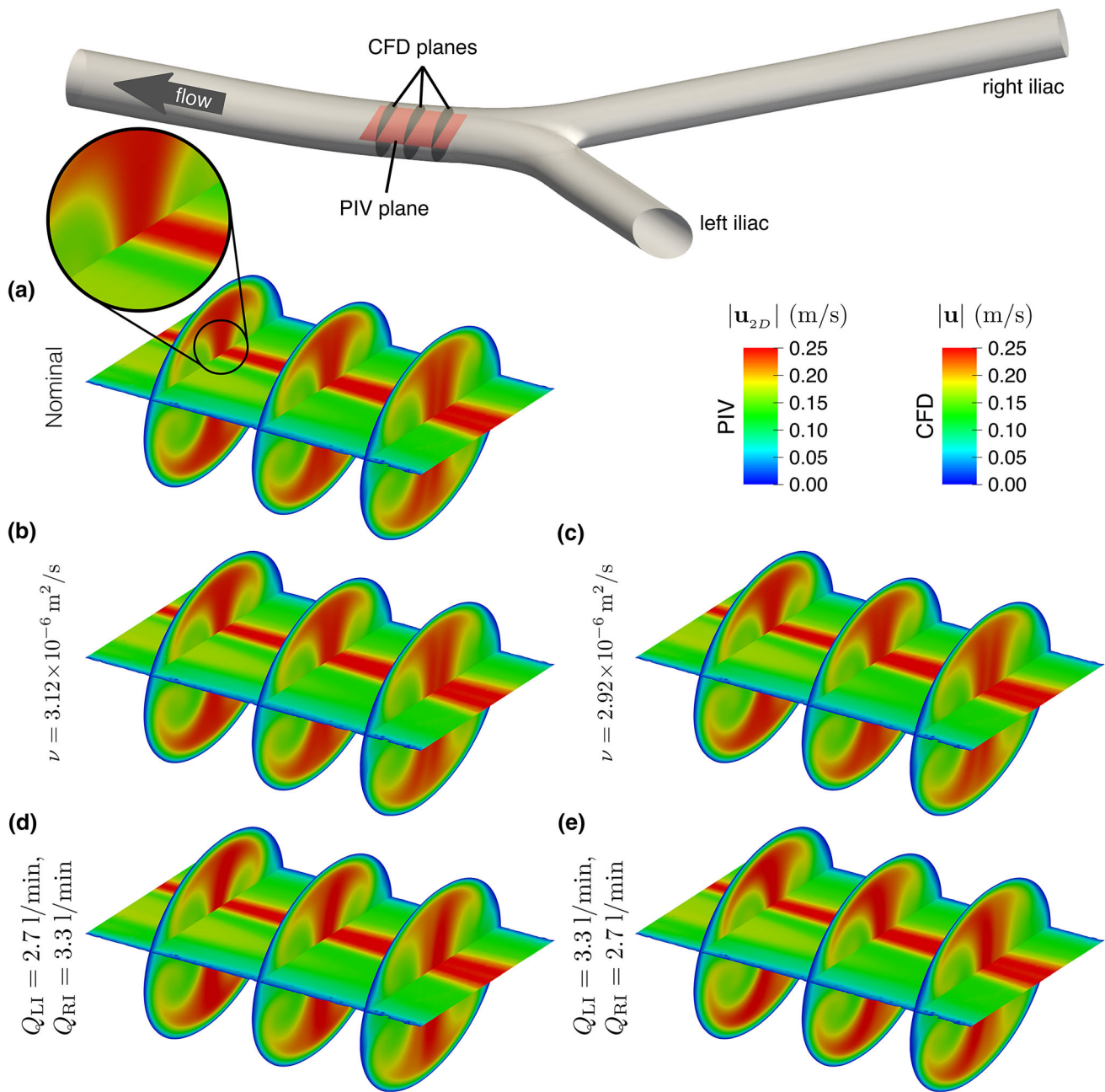


**FIGURE 10.** Influence of input uncertainty on the comparison of qualitative flow patterns between CFD and PIV measurements in the coronal plane at exercise conditions. The CFD solution is shown on transverse planes in the infrarenal IVC from simulations using (a) nominal input parameters, (b) a kinematic viscosity ( $\nu$ ) of  $3.12 \times 10^{-6} \text{ m}^2/\text{s}$  (+3.3%), (c)  $2.92 \times 10^{-6} \text{ m}^2/\text{s}$  (-3.3%), (d) a left iliac flow rate ( $Q_{LI}$ ) of 2.7 l/min (-10%) and a right iliac flow rate ( $Q_{RI}$ ) of 3.3 l/min (+10%), and (e)  $Q_{LI} = 3.3 \text{ l/min}$  (+10%) and  $Q_{RI} = 2.7 \text{ l/min}$  (-10%). Contours of two-dimensional velocity magnitude,  $|u_{2D}|$ , are shown in the coronal plane for PIV and contours of three-dimensional velocity magnitude,  $|u|$ , are shown on transverse cross-sections for CFD.

simulation was shown to accurately predict the same flow speeds and detailed flow patterns observed in the PIV data. Given the complexity of the three-dimensional flow patterns at exercise conditions, the qualitative agreement is excellent. Quantitatively, we show that the global relative comparison error ( $E$ ) between CFD and PIV ranges from 3 to 11% (Table 4). The

largest comparison error is at exercise flow rate conditions in the coronal plane. We show that the quantitative discrepancy in this plane is mostly due to a slight shift in the location of the high velocity region in the center of the IVC lumen in the CFD results compared to the PIV measurements (see Fig. 10a).

Assuming no bias errors in the experiments, the comparison error,  $E$ , between CFD and PIV must be due to either: (i) model error associated with the inherent assumptions or the formulation of the governing equations, (ii) numerical error in the CFD solution of the governing equations (e.g., due to inadequate mesh resolution), (iii) differences in the input parameters between simulations and experiments, or (iv) uncertainties associated with the comparison itself. Given the use of a Newtonian fluid and the observation of laminar flow in the experiments,<sup>11</sup> we have confidence in the applicability of the underlying mathematical model that assumes laminar flow of a Newtonian fluid (Section “[Governing Equations](#)”). Additionally, we performed a rigorous mesh refinement study using a series of eight CFD meshes and demonstrated mesh convergence of the computed solutions and reasonably accurate quantitative predictions with little numerical error associated with inadequate mesh resolution (Section “[Solution Verification: Mesh Refinement Study](#)”). Thus, any discrepancy between CFD and PIV must be due to either uncertainty in the input parameters or is associated with the validation comparison itself. We performed two sensitivity studies to investigate the influence of PIV laser sheet thickness and location (Section “[Sensitivity to PIV Plane Thickness and Location](#)”) and input uncertainty (Section “[Sensitivity to Input Uncertainty](#)”) on the CFD results and the PIV-CFD comparison. We found that small variations of  $\pm 1$  mm in the coronal plane location lead to variations in the relative comparison error of between 1.6 and 3.2%. Uncertainty in the input flow rate to each iliac vein has a slightly larger influence, with variations in  $E$  of between 2.4 and 3.3% when the inlet flow rate is varied by  $\pm 10\%$ , which corresponds to the reported measurement accuracy.<sup>11</sup> Thus, the quantitative discrepancy between CFD and PIV is most likely attributable to a combination of (i) uncertainty in the inlet flow rate to each iliac vein, and (ii) uncertainty associated with precisely aligning the PIV data with the CFD geometry. Nevertheless, the comparison is reasonably good, especially given the complexity of the flow patterns at exercise conditions and the challenges of acquiring PIV data in a complex anatomical model and precisely registering it in the CFD coordinate system.

In future work, we plan to supplement the PIV data set with 3D phase-contrast magnetic resonance imaging (MRI) measurements (e.g., see Refs. 18, 35) in the same model. Using this approach we can simultaneously acquire the geometry and volumetric flow data, allowing us to exactly register the experimental geometry with the CFD model. Additionally, given the 3D velocity field, we can calculate experimental values of secondary quantities such as  $LNH$  and  $\overline{HI}$  for

comparison with CFD. Because an optically transparent model is not required for phase-contrast MRI, we can easily use a non-Newtonian blood analog fluid without the difficulty of also having to match the index of refraction of the 3D printed part. Multiple experimental realizations should be acquired (e.g., see Refs. 13, 15) to quantify the variability in the measurements due to variability in the input parameters. Non-deterministic CFD simulations can then be performed to facilitate a statistical comparison with experimental data and calculation of a quantitative validation metric.<sup>10,22,30</sup>

Finally, there are several implications of the present results regarding IVC filter embolus trapping. From a fluid dynamics perspective, there is significantly more swirl and mixing in the IVC under exercise conditions compared with the resting flow rate condition. Such mixing will likely influence the transport and trapping of emboli by an IVC filter, which will be investigated in future work. Additionally, we found that a relatively fine mesh is required to accurately resolve fine-scale structure in the  $LNH$  field and quantitative values of  $\overline{HI}$ . However, to what extent such small-scale helicity influences embolus transport remains to be determined, and perhaps a coarser mesh is adequate to accurately simulate embolus transport and trapping. This would be advantageous, as predicting the statistics of embolus trapping can require hundreds of separate simulations (e.g., see Refs. 5, 6). In either case, the use of a relatively fine mesh having a resolution comparable to Mesh 6 (see Table 2 and Fig. 3) is anticipated to be an upper limit on the size of the mesh required to accurately predict embolus transport in the IVC under exercise conditions.

## SUMMARY

In this study, we perform solution verification and validation of CFD simulations in a patient-averaged anatomical model of the inferior vena cava (IVC). Because we are most interested in the fluid dynamics in the IVC that influence embolus transport and IVC filter embolus trapping, we focus our analyses on the comparison of the velocity distribution and the amount of swirl and mixing. A mesh refinement study is first conducted to verify that the solutions are mesh-convergent and to quantify the numerical uncertainty at the highest flow rate condition (exercise). Using unstructured hexahedral CFD meshes ranging in size from 800,000 to 102.5 million computational cells, we demonstrate that a relatively coarse mesh may be used to resolve the gross flow patterns and velocity distribution in the IVC. A finer mesh is, however, required to obtain asymptotic mesh convergence of swirl and mixing in the IVC, as quantified by the local normal-



ized helicity ( $LNH$ ) and the volume-averaged helicity intensity ( $\overline{HI}$ ). Based on the results of the mesh refinement study, we chose to use a moderately fine mesh containing approximately 26 million computational cells (Mesh 6) for comparison with the experimental data of Gallagher *et al.*<sup>11</sup> This is because Mesh 6 was shown to adequately resolve both the velocity field and the helicity distribution in the IVC, and to yield reasonably accurate quantitative predictions of the maximum velocity magnitude ( $|\mathbf{u}|_{max}$ ), the area-averaged transverse velocity magnitude ( $\overline{|\mathbf{u}_r|}$ ), and  $\overline{HI}$  with estimated values of numerical uncertainty of 0.24, 2.15, and 2.68%, respectively.

The validation study demonstrated excellent qualitative agreement between the CFD predictions and PIV measurements of the velocity distribution in the infrarenal IVC at both flow rate conditions (rest and exercise). At the resting flow condition, the CFD results closely match the PIV data, aside from a slight difference in the velocity magnitude in the sagittal plane. At the exercise flow rate, the CFD simulation was shown to accurately predict the same flow speeds and detailed flow patterns observed in the PIV data. Given the complexity of the three-dimensional flow patterns at exercise conditions, the qualitative agreement is excellent.

To quantitatively compare CFD and PIV, we calculate the global relative comparison error ( $E$ ), which represents the average percent difference between the computed and measured velocity field. Overall, the quantitative agreement of CFD and PIV is relatively good, with values of  $E$  ranging from 3 to 11%. The largest comparison error is at exercise flow rate conditions in the coronal plane, where there are large out-of-plane velocity gradients. Given our confidence in the applicability of the underlying computational model (laminar flow of a Newtonian fluid) and the small numerical uncertainty predicted as part of our rigorous mesh refinement study, we argue that any discrepancy between CFD and PIV is due to uncertainty in the input parameters or is incurred in the validation comparison itself. By performing sensitivity studies, we demonstrate that, indeed, the quantitative discrepancy is most likely due to (i) uncertainty in the inlet flow rate to each iliac vein, and (ii) uncertainty associated with precisely aligning the PIV data with the CFD geometry.

#### ACKNOWLEDGMENTS

We thank Joshua Sonesson and Tina Morrison for reviewing the manuscript. This study was funded by the U.S. FDA Center for Devices and Radiological

Health (CDRH) Critical Path program. The research was supported in part by an appointment to the Research Participation Program at the U.S. FDA administered by the Oak Ridge Institute for Science and Education through an interagency agreement between the U.S. Department of Energy and FDA. The simulations were performed using the computational resources of the high-performance computing clusters at the U.S. FDA. The findings and conclusions in this article have not been formally disseminated by the FDA and should not be construed to represent any agency determination or policy. The mention of commercial products, their sources, or their use in connection with material reported herein is not to be construed as either an actual or implied endorsement of such products by the Department of Health and Human Services.

#### CONFLICT OF INTEREST

B. A. Craven, K. I. Aycock, and K. B. Manning declare that they have no conflict of interest.

#### ETHICAL APPROVAL

No human studies were carried out by the authors for this article. No animal studies were carried out by the authors for this article.

#### REFERENCES

- <sup>1</sup>ASME V&V 20-2009. Standard for verification and validation in computational fluid dynamics and heat transfer. American Society of Mechanical Engineers, 2016.
- <sup>2</sup>ASME V&V 40-2018. Assessing credibility of computational modeling through verification and validation: application to medical devices. American Society of Mechanical Engineers, 2018.
- <sup>3</sup>Aycock, K. I., R. L. Campbell, K. B. Manning, S. P. Sastry, S. M. Shontz, F. C. Lynch, and B. A. Craven. A computational method for predicting inferior vena cava filter performance on a patient-specific basis. *J. Biomech. Eng.* 136(081):003, 2014.
- <sup>4</sup>Aycock, K. I., R. L. Campbell, F. C. Lynch, K. B. Manning, and B. A. Craven. The importance of hemorheology and patient anatomy on the hemodynamics in the inferior vena cava. *Ann. Biomed. Eng.* 44(12):3568–3582, 2016.
- <sup>5</sup>Aycock, K. I., R. L. Campbell, F. C. Lynch, K. B. Manning, and B. A. Craven. Computational predictions of the embolus-trapping performance of an IVC filter in patient-specific and idealized IVC geometries. *Biomech. Model. Mechanobiol.* 16:1957–1969, 2017a. <https://doi.org/10.1007/s10237-017-0931-5>.
- <sup>6</sup>Aycock, K. I., R. L. Campbell, K. B. Manning, and B. A. Craven. A resolved two-way coupled CFD/6-DOF

- approach for predicting embolus transport and the embolus-trapping efficiency of IVC filters. *Biomech. Model. Mechanobiol.* 16(3):851–869, 2017b. <https://doi.org/10.1007/s10237-016-0857-3>.
- <sup>7</sup>Aycock, K. I., P. Hariharan, and B. A. Craven. Particle image velocimetry measurements in an anatomical vascular model fabricated using inkjet 3D printing. *Exp. Fluids* 58(11):154, 2017c. <https://doi.org/10.1007/s00348-017-2403-1>.
- <sup>8</sup>Caplin, D. M., B. Nikolic, S. P. Kalva, S. Ganguli, W. E. Saad, and D. A. Zuckerman. Quality improvement guidelines for the performance of inferior vena cava filter placement for the prevention of pulmonary embolism. *J. Vasc. Interv. Radiol.* 14:S271–S275, 2011. <https://doi.org/10.1016/j.jvir.2011.07.012>.
- <sup>9</sup>Chiastra, C., S. Morlacchi, D. Gallo, U. Morbiducci, R. Cardenes, I. Larrabide, and F. Migliavacca. Computational fluid dynamic simulations of image-based stented coronary bifurcation models. *J. R. Soc. Interface* 10(84):20130193–20130193, 2013. <https://doi.org/10.1098/rsif.2013.0193>.
- <sup>10</sup>Choudhary, A., I. T. Voyles, C. J. Roy, W. L. Oberkampf, and M. Patil. Probability bounds analysis applied to the Sandia verification and validation challenge problem. *J. Verif. Valid. Uncertain. Quantif.* 1(1):011003, 2016. <https://doi.org/10.1115/1.4031285>.
- <sup>11</sup>Gallagher, M., K. Aycock, B. Craven, and K. Manning. Steady flow in a patient-averaged inferior vena cava—part I: particle image velocimetry measurements at rest and exercise conditions. *Cardiovasc. Eng. Technol.* 2018. <https://doi.org/10.1007/s13239-018-00390-2>.
- <sup>12</sup>Gallo, D., D. A. Steinman, P. B. Bijari, and U. Morbiducci. Helical flow in carotid bifurcation as surrogate marker of exposure to disturbed shear. *J. Biomech.* 45(14):2398–2404, 2012. <https://doi.org/10.1016/j.jbiomech.2012.07.007>.
- <sup>13</sup>Hariharan, P., K.I. Aycock, M. Buesen, S.W. Day, B.C. Good, L.H. Herbertson, U. Steinseifer, K.B. Manning, B.A. Craven, and R.A. Malinauskas. Inter-laboratory characterization of the velocity field in the FDA blood pump model using particle image velocimetry (PIV). *Cardiovasc. Eng. Technol.* 2018. <https://doi.org/10.1007/s13239-018-00378-y>.
- <sup>14</sup>López, J.M., G. Fortuny, D. Puigjaner, J. Herrero, and F. Marimon. A comparative CFD study of four inferior vena cava filters. *Int. J. Numer. Methods Biomed. Eng.* e2990, 2018. <https://doi.org/10.1002/cnm.2990>.
- <sup>15</sup>Malinauskas, R. A., P. Hariharan, S. W. Day, L. H. Herbertson, M. Buesen, U. Steinseifer, K. I. Aycock, B. C. Good, S. Deutsch, K. B. Manning, and B. A. Craven. FDA benchmark medical device flow models for CFD validation. *ASAIO J.* 63(2):150–160, 2017.
- <sup>16</sup>Moffatt, H., and A. Tsinober. Helicity in laminar and turbulent flow. *Annu. Rev. Fluid Mech.* 24(1):281–312, 1992.
- <sup>17</sup>Moffatt, H. K. The degree of knottedness of tangled vortex lines. *J. Fluid Mech.* 35(1):117–129, 1969.
- <sup>18</sup>Morbiducci, U., R. Ponzini, G. Rizzo, M. Cadioli, A. Esposito, F. De Cobelli, A. Del Maschio, F. M. Montevocchi, and A. Redaelli. In vivo quantification of helical blood flow in human aorta by time-resolved three-dimensional cine phase contrast magnetic resonance imaging. *Ann. Biomed. Eng.* 37(3):516–531, 2008. <https://doi.org/10.1007/s10439-008-9609-6>.
- <sup>19</sup>Mukherjee, D., J. Padilla, and S. C. Shadden. Numerical investigation of fluid–particle interactions for embolic stroke. *Theor. Comput. Fluid Dyn.* 30(1–2):23–39, 2016.
- <sup>20</sup>Najjari, M.R., J.A. Hinke, K.V. Bulusu, and M.W. Plesniak. On the rheology of refractive-index-matched, non-Newtonian blood-analog fluids for PIV experiments. *Exp. Fluids* 57(6), 2016. <https://doi.org/10.1007/s00348-016-2185-x>.
- <sup>21</sup>Nicolás, M., V. Palero, E. Peña, M. Arroyo, M. Martínez, and M. Malvè. Numerical and experimental study of the fluid flow through a medical device. *Int. Commun. Heat Mass Transf.* 61:170–178, 2015. <https://doi.org/10.1016/j.icheatmasstransfer.2014.12.013>.
- <sup>22</sup>Oberkampf, W. L., and C. J. Roy. *Verification and Validation in Scientific Computing*. Cambridge: Cambridge University Press, 2010.
- <sup>23</sup>Rahbar, E., D. Mori, and J. Moore, Jr. Three-dimensional analysis of flow disturbances caused by clots in inferior vena cava filters. *J. Vasc. Interv. Radiol.* 22:835–842, 2011.
- <sup>24</sup>Ren, Z., S. L. Wang, and M. A. Singer. Modeling hemodynamics in an unoccluded and partially occluded inferior vena cava under rest and exercise conditions. *Med. Biol. Eng. Comput.* 50(3):277–287, 2012. <https://doi.org/10.1007/s11517-012-0867-y>.
- <sup>25</sup>Roach, M. R., S. Scott, and G. G. Ferguson. The hemodynamic importance of the geometry of bifurcations in the circle of Willis (glass model studies). *Stroke* 3(3):255–267, 1972.
- <sup>26</sup>Roache, P. J. Perspective: a method for uniform reporting of grid refinement studies. *J. Fluids Eng.* 116(3):405–413, 1994.
- <sup>27</sup>Roache, P. J. Quantification of uncertainty in computational fluid dynamics. *Annu. Rev. Fluid Mech.* 29(1):123–160, 1997.
- <sup>28</sup>Roache, P. J. *Fundamentals of Verification and Validation*. Socorro, NM: Hermosa Publishers, 2009.
- <sup>29</sup>Roache, P. J. Verification and validation in fluids engineering: some current issues. *J. Fluids Eng.* 138(10):101205, 2016. <https://doi.org/10.1115/1.4033979>.
- <sup>30</sup>Roy, C. J., and W. L. Oberkampf. A comprehensive framework for verification, validation, and uncertainty quantification in scientific computing. *Comput. Methods Appl. Mech. Eng.* 200(25–28):2131–2144, 2011. <https://doi.org/10.1016/j.cma.2011.03.016>.
- <sup>31</sup>Shtilman, L., E. Levich, S. A. Orszag, R. B. Pelz, and A. Tsinober. On the role of helicity in complex fluid flows. *Phys. Lett. A* 113(1):32–37, 1985.
- <sup>32</sup>Singer, M. A., W. D. Henshaw, and S. L. Wang. Computational modeling of blood flow in the TrapEase inferior vena cava filter. *J. Vasc. Interv. Radiol.* 20(6):799–805, 2009. <https://doi.org/10.1016/j.jvir.2009.02.015>.
- <sup>33</sup>Singer, M. A., and S. L. Wang. Modeling blood flow in a tilted inferior vena cava filter: Does tilt adversely affect hemodynamics? *J. Vasc. Interv. Radiol.* 22(2):229–235, 2011. <https://doi.org/10.1016/j.jvir.2010.09.032>.
- <sup>34</sup>Singer, M. A., S. L. Wang, and D. P. Diachin. Design optimization of vena cava filters: An application to dual filtration devices. *J. Biomech. Eng.* 132(10):101006, 2010. <https://doi.org/10.1115/1.4002488>.
- <sup>35</sup>Sotelo, J., J. Urbina, I. Valverde, J. Mura, C. Tejos, P. Irrarrazaval, M. E. Andia, D. E. Hurtado, and S. Uribe. Three-dimensional quantification of vorticity and helicity from 3D cine PC-MRI using finite-element interpolations.

- Magn. Reson. Med.* 79(1):541–553, 2018. <https://doi.org/10.1002/mrm.26687>.
- <sup>36</sup>Stewart, S. F. C., R. A. Robinson, R. A. Nelson, and R. A. Malinauskas. Effects of thrombosed vena cava filters on blood flow: flow visualization and numerical modeling. *Ann. Biomed. Eng.* 36(11):1764–1781, 2008. <https://doi.org/10.1007/s10439-008-9560-6>.
- <sup>37</sup>Swaminathan, T., H. H. Hu, and A. A. Patel. Numerical analysis of the hemodynamics and embolus capture of a Greenfield vena cava filter. *J. Biomech. Eng.* 128(3):360–370, 2006.
- <sup>38</sup>Tedaldi, E., C. Montanari, K. I. Aycock, F. Sturla, A. Redaelli, and K. B. Manning. An experimental and computational study of the inferior vena cava hemodynamics under respiratory-induced collapse of the infrarenal IVC. *Med. Eng. Phys.* 54:44–55, 2018. <https://doi.org/10.1016/j.medengphy.2018.02.003>.
- <sup>39</sup>Wang, S. L., and M. A. Singer. Toward an optimal position for inferior vena cava filters: computational modeling of the impact of renal vein inflow with Celect and TrapEase filters. *J. Vasc. Interv. Radiol.* 21(3):367–374, 2010. <https://doi.org/10.1016/j.jvir.2009.11.013>.
- <sup>40</sup>Yap, C. H., X. Liu, and K. Pekkan. Characterization of the vessel geometry, flow mechanics and wall shear stress in the great arteries of wildtype prenatal mouse. *PLoS ONE* 9(1): e86878, 2014. <https://doi.org/10.1371/journal.pone.0086878>.